JOURNAL OF SOLID STATE CHEMISTRY **23**, 59–71 (1978)

Calculated n-Beam Crystal Structure Images of Oxides Based on Fluorite and ReO_3 and the Interpretation of Observed Images*

A. JEROME SKARNULIS, E. SUMMERVILLE,† AND LEROY EYRING‡

Department of Chemistry and the Center for Solid State Science, Arizona State University, Tempe, Arizona 85281

Received May 9, 1977

Dynamical n-beam calculations are used to explore the potential of crystal structure imaging for investigating superstructures in fluorite-related systems. Crystal structure images of M_7O_{12} phases are investigated under various conditions of crystal thickness and defect of focus, and it is shown that under some conditions crystal structure images show direct structural correlation. In others where the structural correlation is missing the calculated and observed images still agree. Two programs, FCOEFF and DEFECT, which allow calculation of images of structures with any symmetry and in any projection, are tendered. The n-beam calculations on a number of ReO_3-based structures are also presented to demonstrate the versatility of the programs.

Introduction

Many tensimetric and X-ray studies of the binary rare earth oxide systems of Ce, Pr, and Tb have been carried out (*1*) to reveal the nature of the ordering phenomena in these materials. These systems have been of considerable interest because of the presence of a homologous series of ordered phases of general formula R_nO_{2n-2} with observed n values of 4, 7, 9, 10, 11, 12, and ∞. Each phase is closely related structurally to fluorite and successive members of the series differ only in the proportion and arrangement of vacant fluorite anion sites. At equilibrium, each phase has a narrow range of homogeneity and a high degree of order. Since any description of the properties of these systems is impossible without taking due regard of the ordering processes in the system, detailed structural information on the intermediate phases is essential.

In a previous article, Kunzmann and Eyring (*2*) described the unit cells of each of the intermediate phases and, with the aid of a crystal structure image of $Tb_{11}O_{20}$, proposed a structural model for the odd-member phases. However, application of high resolution crystal structure imaging to fluorite-type structures had not been previously attempted, so its applicability and the validity of interpretation of such images in terms of vacancies were uncertain.

Many previous electron microscopic studies using high resolution crystal structure imaging have involved block structures where the subcell is that of the ReO_3 structure-type (Allpress and Sanders (*3*)). This subcell exhibits large variations in potential when viewed down the b axis because it consists of columns of corner-sharing MO_6 octahedra within which the potential is very high and outside of which it is extremely low. The

---

* Work supported by the United States Energy Research and Development Administration.

† Present address: School of Physical Sciences, Flinders University of South Australia, Bedford Park 5042, South Australia.

‡ Author to whom inquiries should be addressed.

0022-4596/78/2312-0059 $02.00/0

Printed in Great Britain

supercells of the ordered phases are then derived from this structure by crystallographic shear (*CS*), one result of which is a sharp increase in concentration of cations in the vicinity of the *CS* plane. Again large, localized variations in potential are produced parallel to the *b* axis of the subcell.

In contrast, the fluorite superstructures have little to recommend them for crystal structure imaging. The parent fluorite structure has few projection directions which would exhibit large potential variations on a scale comparable to the resolution limit of an electron microscope (the most favorable direction would be $[110]_F$). Since the supercells are formed from the parent structure by ordering of vacant anion sites with associated relaxation of the host structure, it is unlikely that ordering would produce any major changes in the projected potential. A further disadvantage in imaging these phases is that any projection axis will be rather long, ranging from 6.75 Å for a $[100]_7$ axis (the subscript refers to the value of *n* in the homologous series R_nO_{2n-2}) to 9.6 Å for a $[111]_7$ axis. Such long axes strain the thin phase object approximation used in calculating the images and minimize the magnitude of potential variations due to vacancy ordering. At the same time, reciprocal-lattice axes perpendicular to the projection axis are also disadvantageously long, so that with reasonable aperture sizes the images are produced from the interaction of a undesirably small number of beams.

In view of these unfavorable circumstances it seems necessary that calculations of image contrast be made to support intuitive interpretation of the observed crystal structure images. The details of such calculations have been described previously by Allpress *et al.* (*4*) and O'Keefe (*5*). The most accurate method of incorporating dynamical diffraction effects, the *n*-beam multislice method of Cowley and Moodie (*6*, *7*), was selected for this study. Since the structure of only one of the intermediate phases ($n = 7$, iota) is known (*8*) detailed calculations can only be performed on this phase. Nevertheless, it is thought that the conclusions reached in this case will aid interpretation of the observed images of the other homologs. It is fortuitous that the structure is known for that phase which appears to be the structural, if not the compositional, end-member of the homologous series.

Experimental Part

Hydrothermally grown single crystals of PrO_2 (*9*) were ground under liquid nitrogen, placed in a loosely closed platinum capsule which was immersed in a large bed (~30 g) of PrO_x powder, and the mixture reduced to the required composition by adjusting the ambient oxygen pressure at temperature. The sample was then isolated and cooled at constant composition. Grinding of the crystals prior to reduction had the advantages of (a) allowing more rapid equilibration of the crystals with the gas phase, (b) allowing strains induced during grinding to be annealed out, and (c) minimizing the possibility of compositional changes after annealing.

The reduced samples were mounted on a holey carbon support film via an acetone slurry and examined by means of conventional techniques on a modified JEM 100B electron microscope utilizing procedures described by Iijima (*10*).

Calculations

Two FORTRAN programs, FCOEFF and DEFECT, were written to permit calculation of crystal structure images and to provide sundry other information on any structure.

The Program FCOEFF is used to calculate the real, imaginary, and absorption structure factors needed for Program DEFECT. The absorption factors can be assigned for particular atoms by using a specified percentage of the real part. Either isotropic or anisotropic temperature factors for individual atoms may be used.

FCOEFF permits projecting the structure down any direction, [*uvw*], by automatically transforming the three-dimensional indices into a two-dimensional array. The input includes fractional coordinates, symmetry operators, scattering tables, and lattice parameters. The output includes structure factors, three-dimensional and two-dimensional indices, a transformation matrix, new x and y axes, and the plane angle of projection.

The Program DEFECT enables calculation of the theoretical electron micrographs by dynamical theory using the multislice method. It utilizes real, imaginary, and absorption structure factors to calculate images of dislocations, interstitials (*11*), and overlay structures (two layers of the same structure but with different composition superimposed). The program can be run in various configurations: (1) utilizing all the options requires 60K (decimal) UNIVAC words of core without overlaying the program; (2) if the absorption potential calculation is eliminated, the program requires 50K (decimal) words of core; and (3) eliminating the overlay structure calculation and reducing the total number of beams would require less than 40K (decimal). The approximate running time for a 60K (decimal) run of 12 slices, 150 beams, and 257 structure factors is ≈47 SUPS (standard units of processing, UNIVAC 1110, approximately 4000 SUPS/hr).

The input to DEFECT is a punched deck of structure factors from FCOEFF and experimental parameters such as crystal thickness, aperture radius, and the spherical aberration constant.

An excellent description of the multislice method and the relationship to other formulations is given by Goodman and Moodie (*12*). Program DEFECT Fourier transforms the structure factors obtained from FCOEFF to give the crystal potential averaged along the incident direction

$$\phi(x,y) = \sum_{h,k} V(h,k,0)\exp\left(-2\pi i\left(\frac{hx}{a} + \frac{ky}{b}\right)\right).$$

The crystal potential is used to determine the transmission function (the phase change of the diffracted beams as they pass through one slice of the crystal),

$$q(x,y) = \exp(-i\sigma\phi(x,y)\,\Delta z),$$

where $\phi(x, y)$ is the crystal potential, Δz is the slice thickness, and

$$\sigma = \frac{\pi}{W\lambda}\cdot\frac{2}{1+(1+\beta^2)^{1/2}},$$

where W is the accelerating voltage, λ is the relativistic wavelength of the incident electrons with velocity v, and $\beta = v/c$.

The diffraction of the electron beam between the slices is calculated by convoluting the wave equation with the propagation function

$$p(r,\Delta z) = \frac{i}{\Delta z\lambda}\exp\left(\frac{-i\pi r^2}{\lambda\Delta z}\right)$$

so that the wave equation in real space is represented by

$$\Psi(r,z_{n+1}) = q(r)\cdot[\Psi(r,z_n) * p(r,\Delta z)].$$

The equivalent equation in reciprocal space becomes

$$\Psi_{n+1}(h) = Q(h) * [\Psi_n(h)\cdot P_{\Delta z}(h)],$$

where the capital letters are the Fourier transforms of their lower case counterparts,

$$P_{\Delta z} = \exp(i\pi\lambda\Delta z u^2) \qquad \text{where } u^2 = \left(\frac{h^2}{a^2}+\frac{k^2}{b^2}\right)$$

for an orthogonal unit cell. In reciprocal space the convolutions become simple summations instead of integrations yielding

$$\Psi_{n+1}(h) = \sum_{h'} Q(h-h')P_{\Delta z}(h')\,\Psi_n(h')$$

which can be represented physically as a diffracted beam with wave equation $\Psi_n(h')$ entering a slice of crystal and having its phase changed by the effect of the potential encountered in that slice and by the distance it has moved through space. This calculation is repeated until the number of slices corresponds to the crystal thickness.

The program simulates an objective aperture and determines which of the diffracted beams pass through and contribute to the intensity of the image. The phase changes due to defocus,

$$\Psi_R(h,k) = \Psi(h,k)\exp(i\pi\lambda R u^2)$$
$$= \Psi(h,k)\exp\left(i\pi\lambda R\left(\frac{h^2}{a^2}+\frac{k^2}{b^2}\right)\right),$$

where R is the amount of defocus, and to spherical aberration,

$$\Psi_T(h,k) = \Psi_R(h,k)\exp(i\pi/2\lambda^3 C_S u^4)$$
$$= \Psi_R(h,k)\exp\left(i\pi/2\lambda^3 C_S\left(\frac{h^2}{a^2}+\frac{k^2}{b^2}\right)^2\right),$$

where C_S is the spherical aberration coefficient, are applied to the diffracted beams that contribute to the image. Once the amplitudes and phases of all the diffracted beams have been calculated for a particular thickness, a series of corrections corresponding to different degrees of underfocus can be applied and the images can be obtained with little additional computation.

The effect of chromatic aberration is determined by averaging the intensity of the image over a range of defocus (not the amplitudes since electrons of different energies will not interfere coherently (*13*)).

In practice it is possible to perform one multislice calculation for a thick crystal and to punch out the amplitudes and the phases of the diffracted beams at selected intermediate thicknesses. These can be input to DEFECT and images calculated without the need for repeating the multislice calculations.

The final image is then displayed either on a line printer with overprinting or on a graphics terminal. The output of the program includes an overprinted image of the projected potential, an alphanumeric phase map (showing

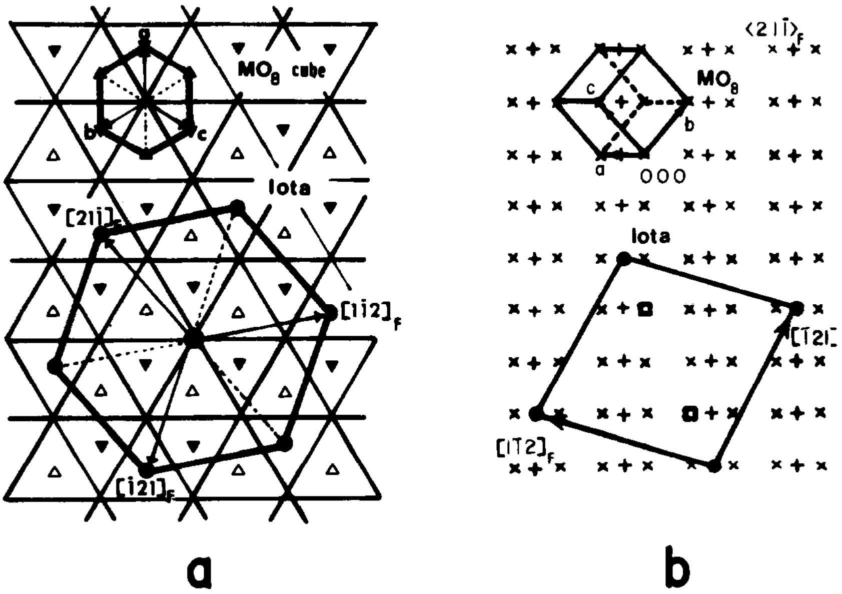

FIG. 1. Projections of the ideal atom positions of Pr_7O_{12} down: (a) The $[111]_F$ axis where the line intersections, filled triangles, and empty triangles represent columns of metal and nonmetal sites at relative intervals of $\frac{1}{12}[111]_F$ to each other. The columns of nonmetal vacancies and six-coordinated metal atoms are indicated by filled circles. (b) The $[211]_F$ axis where metal atom sites are marked with a plus sign, the nonmetal sites are marked by a multiplication sign, nonmetal vacancies are marked with a square, and filled circles again indicate columns of six-coordinated metal atoms. MO_8 cubes are also outlined to facilitate interpretation.

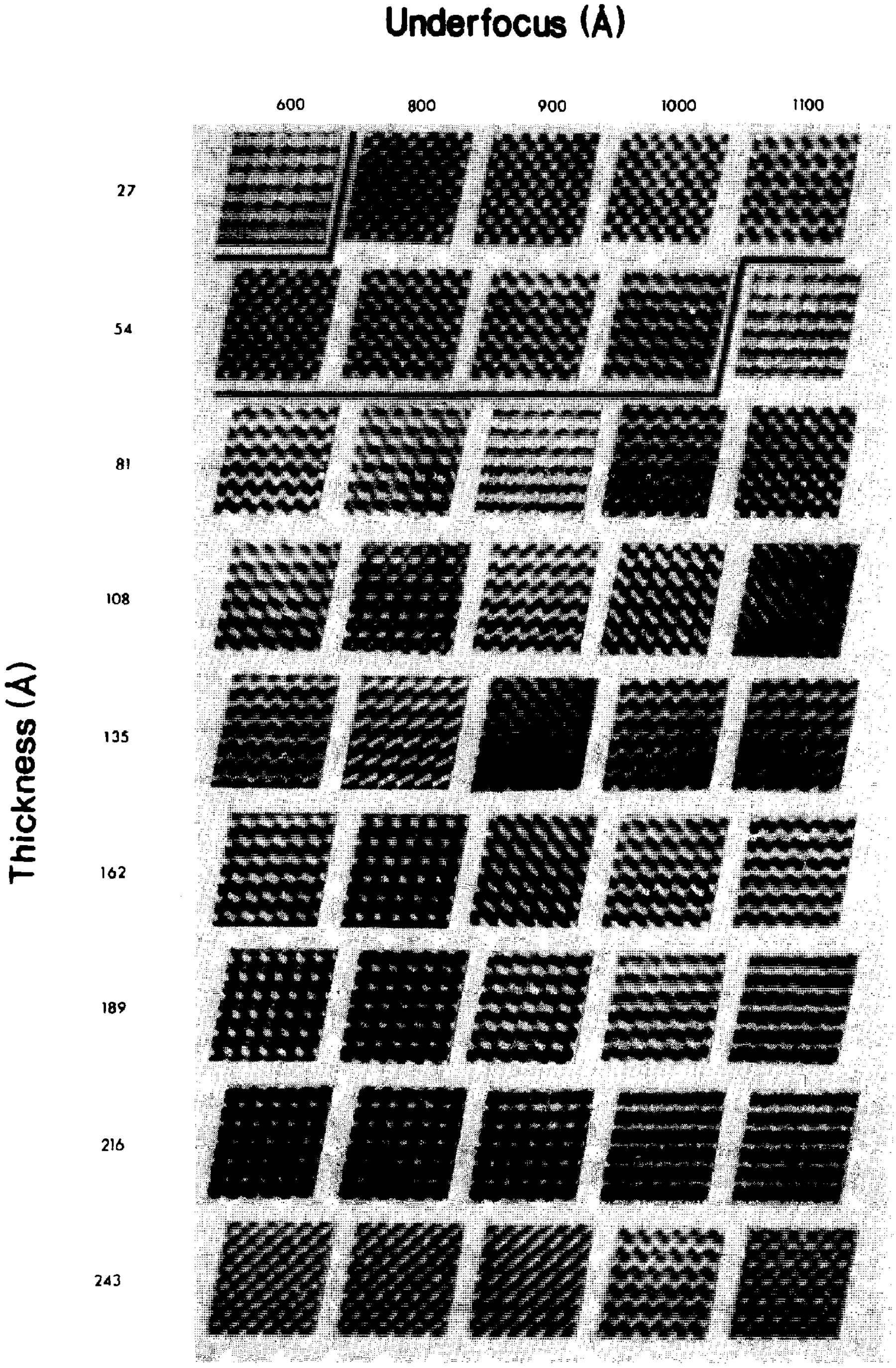

FIG. 2. Calculated *n*-beam crystal structure images for the $\langle 100 \rangle_7$ zone of Pr_7O_{12}. Calculations were made with atomic scattering factors (6 × 6 unit cells).

areas of maximum phase change), a convolution test, a normalization parameter, integrated intensities, and the calculated images at different values of defocus. Plots of amplitudes and phases of diffracted beams versus crystal thickness can also be obtained.

Observations and Correlations

Calculated Images

1. $\langle 21\bar{1}\rangle_F = \langle 100\rangle_7$ *Images*

a. Iota (Pr_7O_{12}). The difference in potential distribution of this phase and that of the parent fluorite structure arises because of the presence of anion vacancies (*V*) and the attendant dilation of the cations of the VM_4 coordination tetrahedra. These two effects result in a significant (though not major) decrease in electrostatic potential in the vicinity of an anion vacancy. If, therefore, a crystal structure image reproduces the variations of potential across a unit cell, one could hope to see evidence of these "vacancies." Figure 1 shows projections of the ideal atom positions of Pr_7O_{12} when viewed down the $\langle 111\rangle_F$ and $\langle 21\bar{1}\rangle_F$ axes (*8*). An MO_8 coordination cube is also outlined in each case to facilitate interpretation of the geometry.

A series of *n*-beam crystal structure images are shown in Fig. 2; variation of the images with defect of focus is shown across the top and variation with thickness down the side. The conditions used to calculate these images were: number of beams = 300; aperture radius = 0.263 Å^{-1}; spherical aberration constant = 1.8 mm; depth of focus = 250 Å. The origin is situated at the top left-hand corner of the figure with two of the axes ($a \equiv b \equiv c$) along the edges of the figure. A six-coordinate cation is located at the origin.

A number of comments should be made about these calculated images. There are two general types of recurrent images—one with an array of spots which is similar to the arrangement of vacancies (two spots per unit cell), the other in which the arrangement of spots is similar to the arrangement of six-coordinated cations (one spot per unit cell). The "vacancy" image type is calculated only for thinner crystals of 100 Å or less, as may be seen in Fig. 2. In these cases the spot arrangement corresponds directly to that of the vacancies (i.e., with the projected potential).

The second type of image calculated has one spot per unit cell located at the origin provided the underfocus is close to 900 Å and occurs for thicknesses of 162–216 Å. These spots represent the six-coordinated cation array although there is no obvious correlation between the projected potential and this image type. Since these images are observed in thicker crystals they cannot be regarded as crystal structure images in the conventional sense because they do not represent the projected potential. Nevertheless, the observed images can be directly correlated with some of the calculated images even though a direct correlation of white spots with structural features, as has been done with the block structures, would not be justified.

In Fig. 3 the intensities and phases of three beams are plotted—one the direct beam, another a subcell reflection, and the third a supercell reflection. The figure shows that the intensity of the diffracted beams is essentially out of phase with the direct beam, which is to be expected, but that the phases are uncorrelated. It seems that a true vacancy image could only be expected with crystal thicknesses up to that of the first extinction—a situation that was probably rarely achieved experimentally.

b. $Zr_3Sc_4O_{12}$. This phase is isostructural with Pr_7O_{12} and hence any differences in the respective images would be due largely to the different form factors of the cations. The images depicted in Fig. 4 were calculated using atomic scattering factors. The Zr and Sc are random on metal positions in the structure determined by Thornber *et al.* (*14*). As in the case of Pr_7O_{12} calculated thin crystal images correlate well with the projected potential (e.g., 24–48-Å thickness, 900–1100-Å underfocus) showing two spots per unit cell corresponding to the vacancies. There are also two spots per unit cell with an origin shift in the thicker

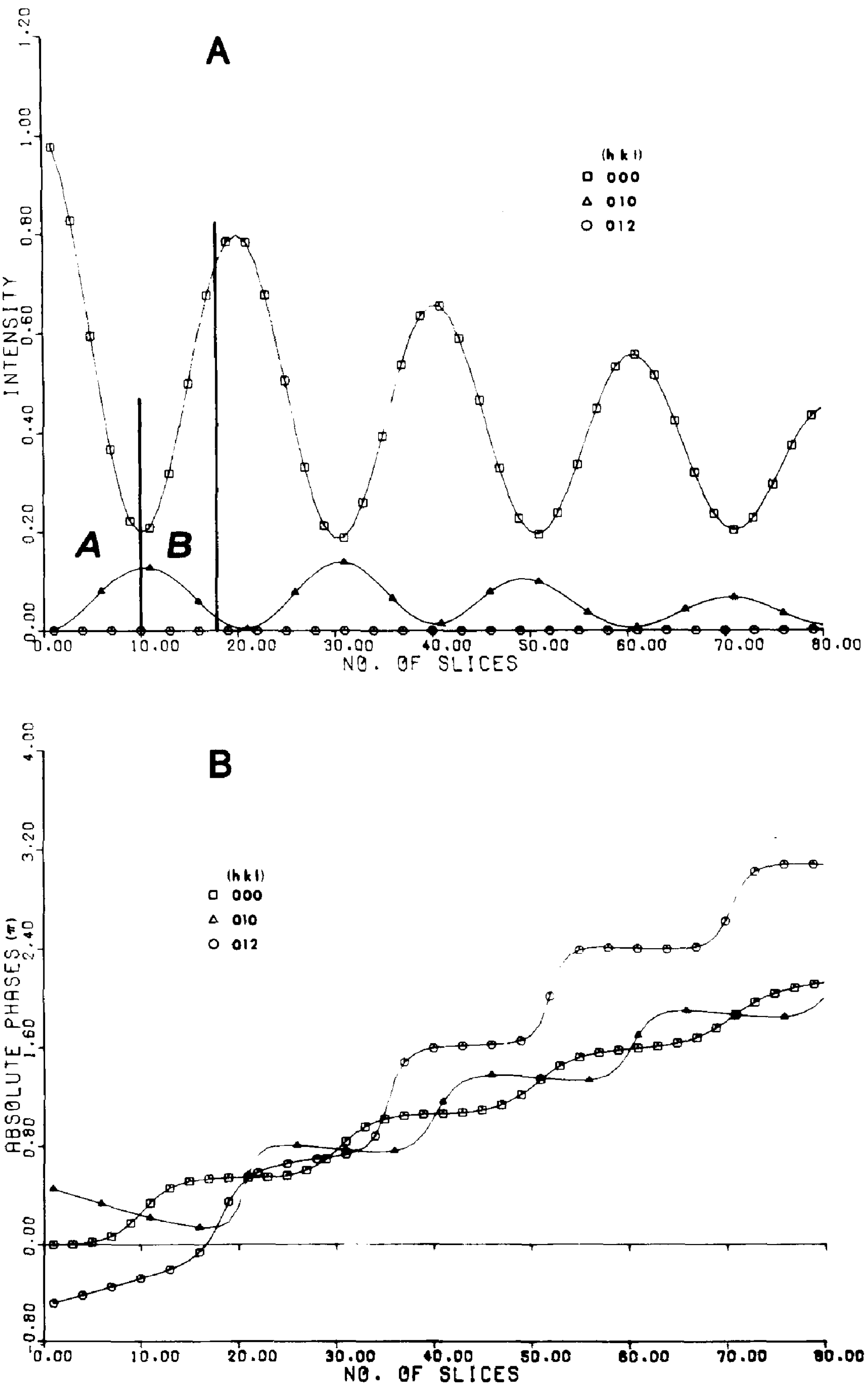

FIG. 3. Plots of (a) intensities and (b) absolute phases of a number of beams in a $\langle 100\rangle_7$ zone of Pr_7O_{12} as a function of crystal thickness. The direct beam is 000, 010 is a subcell reflection, and 012 is a supercell reflection (1 slice = 6.75 Å).

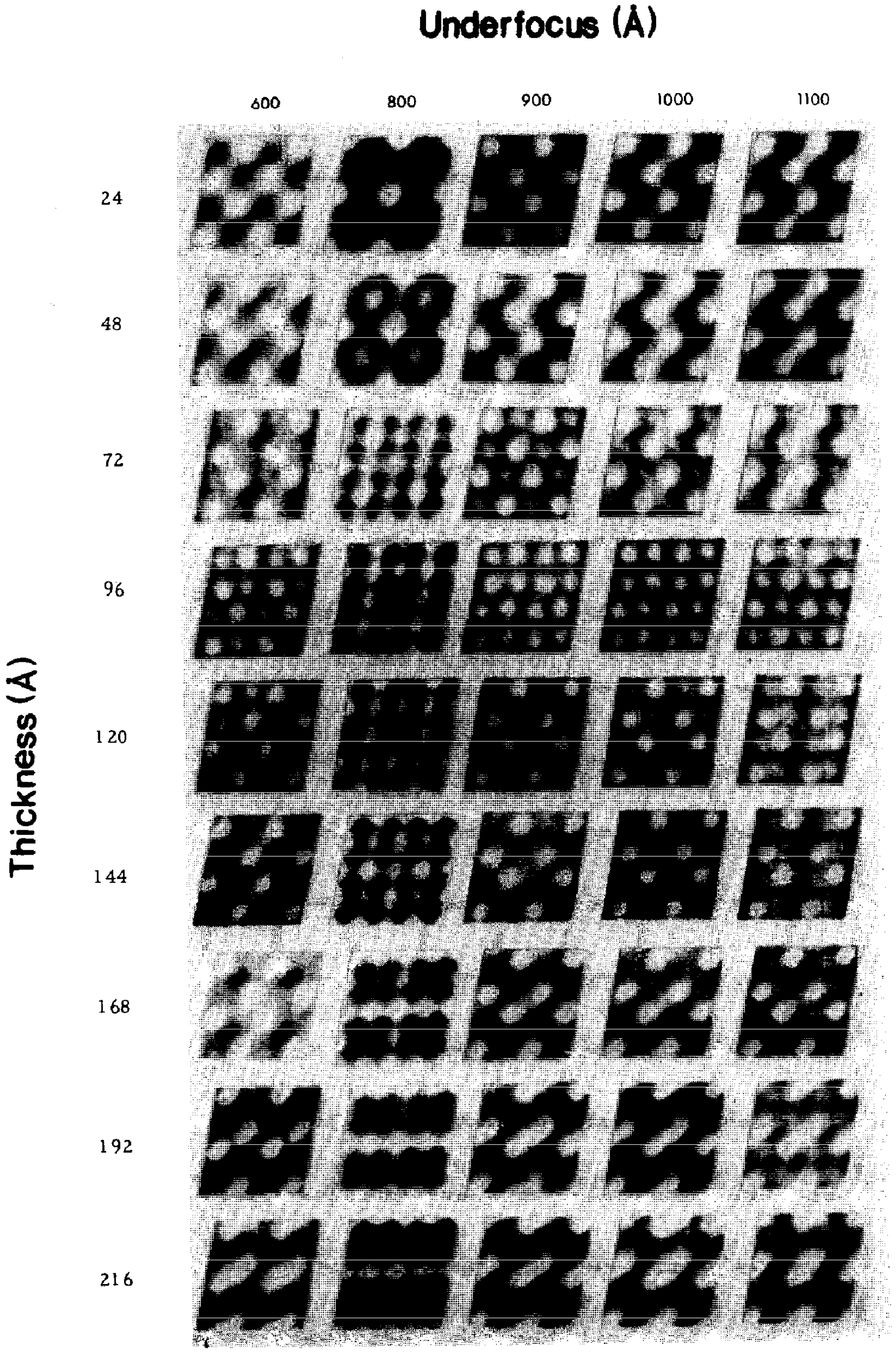

FIG. 4. Calculated n-beam $\langle 100 \rangle_7$ crystal structure images for the $\langle 100 \rangle_7$ zone of $Zr_3Sc_4O_{12}$. Calculations were made with atomic scattering factors (2 × 2 unit cells).

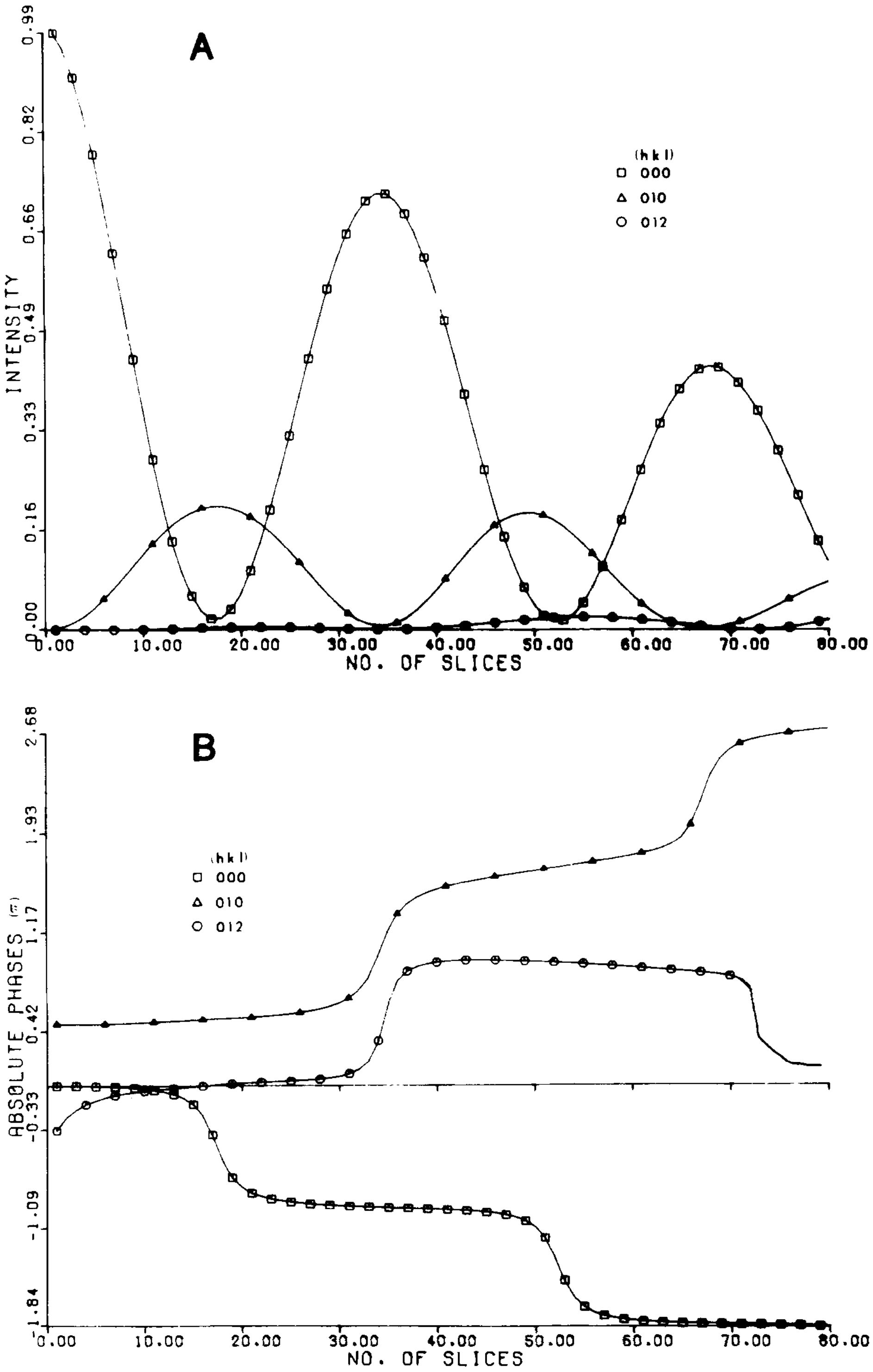

FIG. 5. Plots of (a) intensities and (b) absolute phases of a number of beams in a $\langle 100 \rangle_7$ zone of $Zr_3Sc_4O_{12}$ as a function of crystal thickness. The direct beam is 000, 010 is a subcell reflection, and 012 is a supercell reflection (1 slice = 6.144 Å).

images (e.g., 120–168-Å thicknesses, 900–1100-Å underfocus). It can be seen that the main features in Fig. 4 are qualitatively similar to those of Fig. 2 for Pr_7O_{12}.

Figure 5 shows plots of intensities and phases of three beams—one the direct beam, another a subcell reflection, and the third a supercell reflection. The results resemble those of Pr_7O_{12}, however, the extinction thickness for $Zr_3Sc_4O_{12}$, which results from the low scattering factor of scandium, is greater. One consequence of the increased extinction thickness is the extended region over which any image type is identifiable.

The calculated crystal structure images for $Zr_3Sc_4O_{12}$ also show how the "vacancy" image fades out as an equivalent array, with an origin shift of $b/2$, appears. This phenomenon can be interpreted as a contrast reversal (a phase change of π) for the stronger reflections, as in the Fourier images for simple structures (7). It is likely that the scattering factors should be modified to reflect some ionic character but techniques to do this properly have not been found (*15*). Such a consideration might account for the appearance of the reversal in the calculated images in $Zr_3Sc_4O_{12}$ but not in Pr_7O_{12}.

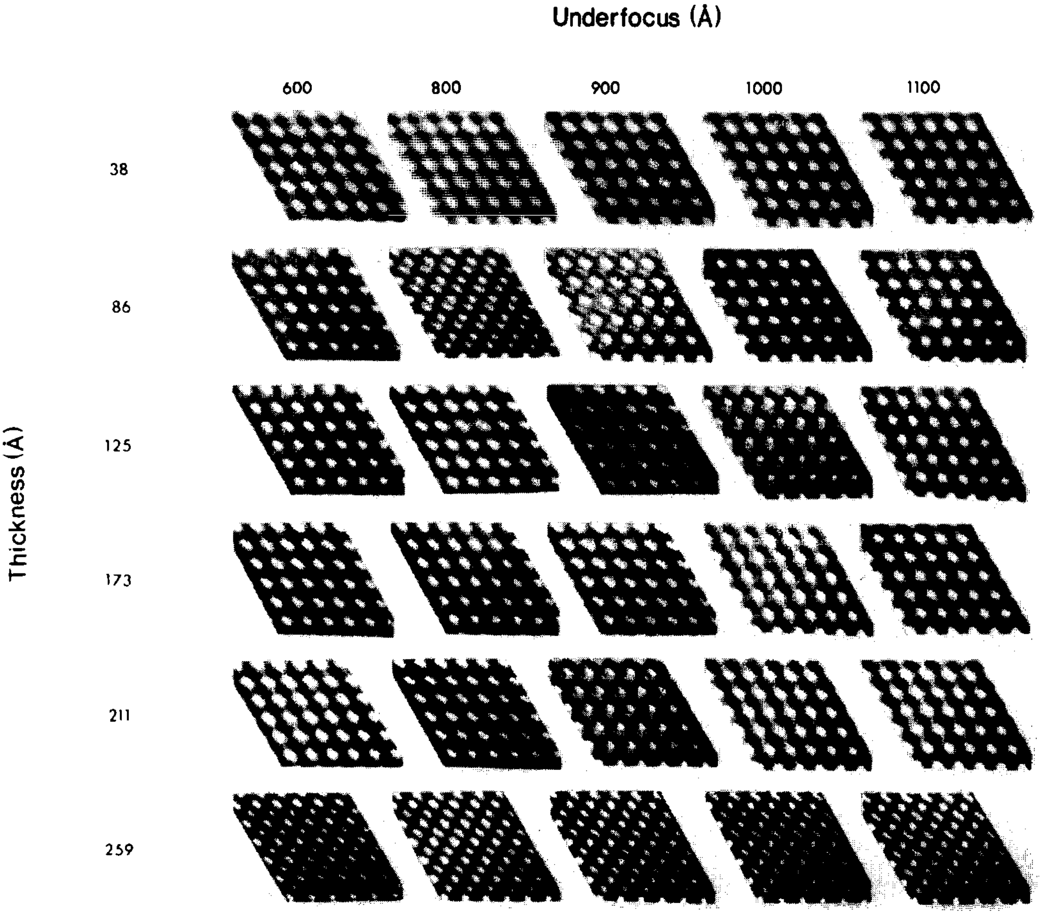

FIG. 6. Calculated $\langle 111 \rangle_7$ crystal structure images of Pr_7O_{12} showing variation with crystal thickness and defect of focus (6 × 6 unit cells).

2. $\langle 111\rangle_7$ *Images of* Pr_7O_{12}

These calculated images (Fig. 6) usually show one spot per unit cell. However, as in a $\langle 100\rangle_7$ zone of $Zr_3Sc_4O_{12}$ there are two arrays of spots, depending on thickness of specimen, both of which correlate with the iota phase structure. The first image type has spots located over the columns of six-coordinated cations and anion vacancies, the second has an identical array but shifted by $b/2 + c/2$ to the center of the projected unit cell. In any experimental image it would not be possible to determine which array was being observed. However, in most cases this would not affect the intuitive interpretation of an image.

3. *Calculated and Observed Images of Other Structures*

Figure 7 compares images previously observed and published by Iijima and those calculated by the methods described here. These structures cover a variety of space groups and demonstrate the versatility of the FCOEFF–DEFECT combination.

4. *Observed Crystal Structure Images*

a. $\langle 100\rangle_7$ *images of* M_7O_{12} *phases.* All observed images of Pr_7O_{12} at ≈900-Å underfocus exhibit only one spot per unit cell so that in no case was a crystal thin enough for observation of anion vacancies. Since this phase is highly isotropic and since its cleavage is conchoidal it is quite likely that edges were never thinner than 100 Å. Most images show only circular spots although a few thicker specimens showed either elliptical spots or streaking. Images showing these features are presented in Figs. 8a and b; Fig. 8c is an image of $Zr_3Sc_4O_{12}$ which shows two spots per unit cell toward the edge and compares quite favorably with the calculated images (144–168 Å thick with −900 to −1000 Å defocus).

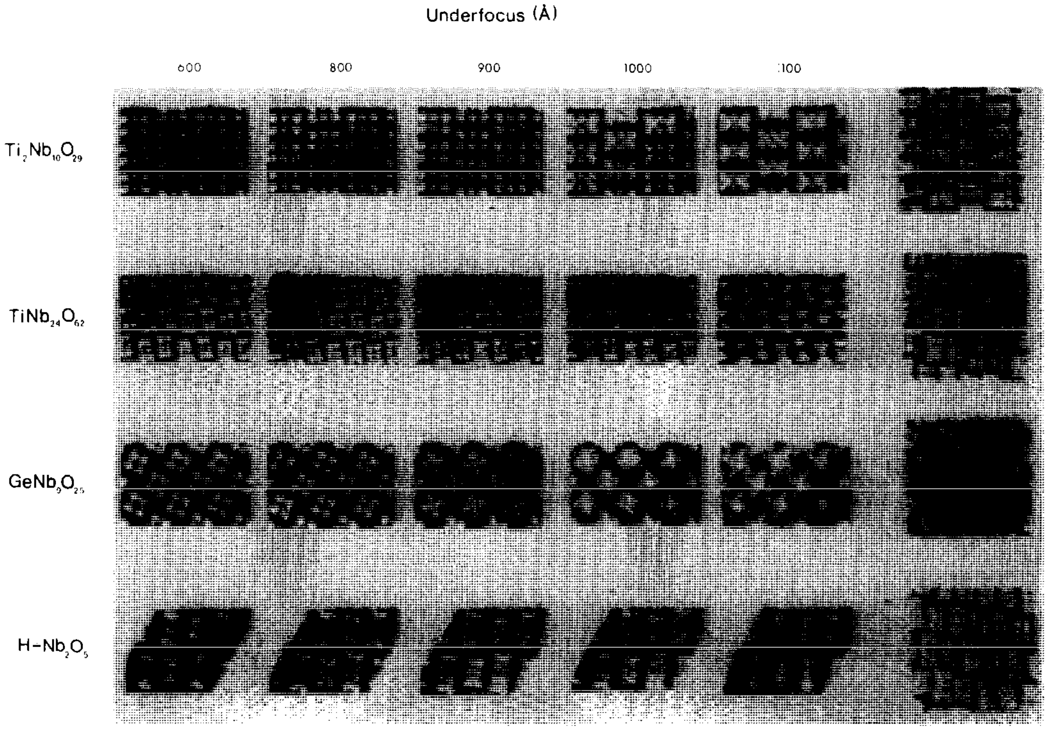

FIG. 7. Computed and experimental crystal structure images of some ReO_3-based superstructures. The experimental images were generally made for crystals about 50 Å thick using 100 beams.

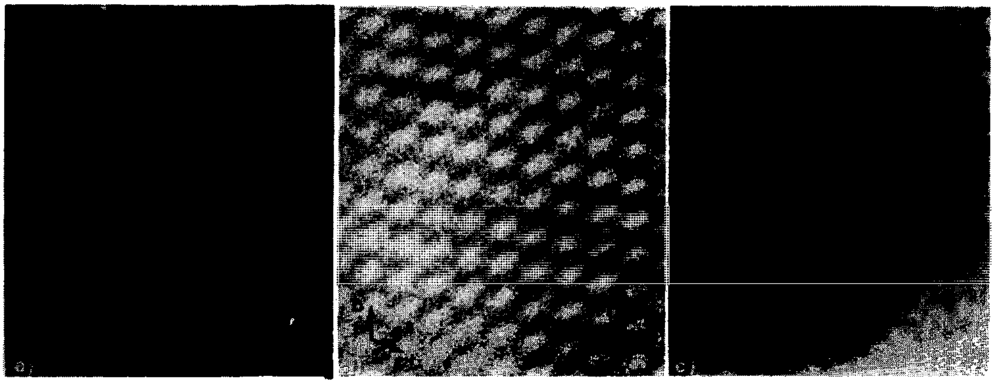

FIG. 8. Observed $\langle 100 \rangle_7$ images of Pr_7O_{12} and $Zr_3Sc_4O_{12}$: (a) a typical image of Pr_7O_{12}; (b) a thick-crystal image of Pr_7O_{12}; and (c) a thin-crystal image of $Zr_3Sc_4O_{12}$ showing the vacancy arrangement.

b. $\langle 111 \rangle_F \equiv \langle 111 \rangle_7$ *images.* These images (Fig. 9a) are quite comparable to those calculated. There seems to be no reason why the white spots should not be directly interpreted in terms of columns of six-coordinated cations and anion vacancies, even though the actual columns may be shifted by $b/2 + c/2$ from the white spots. In Fig. 9b two twin orientations of $Zr_3Sc_4O_{12}$ are shown with a region of C-type sesquioxide in between. The [111] zone axis lies in common for all phases and the image could be favorably compared to the calculated images of the [111] zone.

Conclusions

Comparison of observed and calculated images of Pr_7O_{12} and $Zr_3Sc_4O_{12}$ has shown

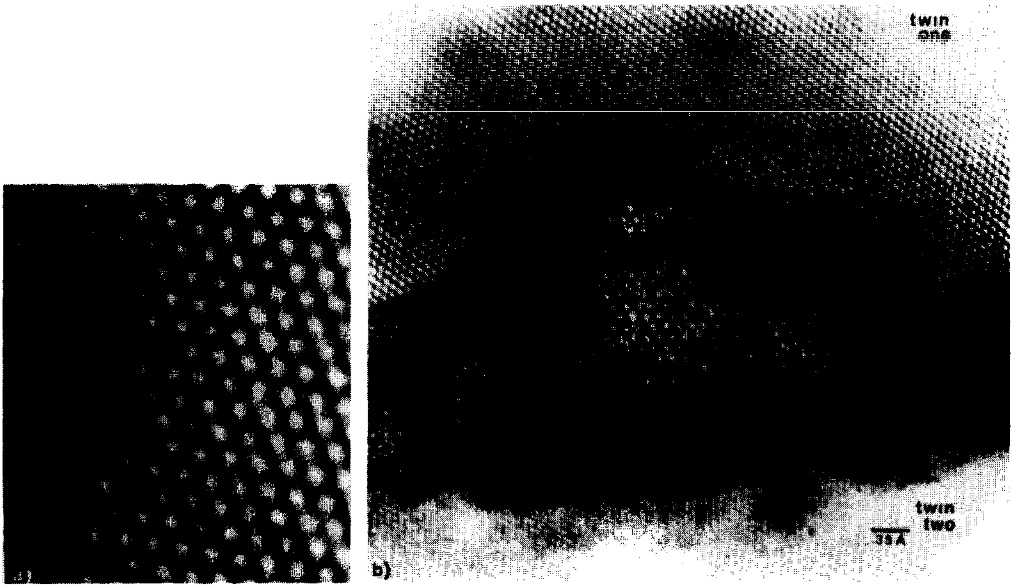

FIG. 9. Observed $\langle 111 \rangle_7$ images of Pr_7O_{12} and $Zr_3Sc_4O_{12}$: (a) a typical image; (b) two twin orientations of $Zr_3Sc_4O_{12}$ separated by a region of C type.

that the technique of crystal structure imaging may be successfully applied to fluorite oxides provided certain limitations are appreciated. Under the experimental conditions used in this study there appears to be no direct correlation between projected potential and the images, either observed or calculated. However, in the thick crystal images there is a close relationship between structure and image and there are no known cases of conflict between the observed and calculated images. It seems possible, therefore, to utilize the observed images to derive possible models for phases of unknown structure and to select the correct one by comparing observed and calculated crystal structure images.

Using atomic scattering factors and assuming thin crystals, images are calculated which reflect the projected potential and spots in the image correlate with the positions of oxygen vacancies unless shifted by a half unit cell. The crystals prepared for this study are too thick to confirm unambiguously agreement between images calculated and observed for thin crystals.

Acknowledgments

We appreciate helpful discussions with J. M. Cowley and R. T. Tuenge. S. Iijima generously provided observed crystal structure images for Fig. 7. We are grateful to K. H. Lau who grew the PrO_2 single crystals from which the specimens of Pr_7O_{12} were prepared. We wish especially to acknowledge the provision, by the University, of computer facilities for the development of the image calculation programs and for their use.

References

1. L. EYRING, *in* "Solid State Chemistry" (C. N. R. Rao, Ed.), pp. 565, Marcel Dekker, New York (1974).
2. P. KUNZMANN AND L. EYRING, *J. Solid State Chem.* **14**, 229 (1975).
3. J. G. ALLPRESS AND J. V. SANDERS, *J. Appl. Crystallogr.* **6**, 165 (1973).
4. J. G. ALLPRESS, E. A. HEWAT, A. F. MOODIE, AND J. V. SANDERS, *Acta Crystallogr.*, Sect. *A* **28**, 528 (1972).
5. M. A. O'KEEFE, *Acta Crystallogr.*, Sect. *A* **29**, 389 (1973).
6. J. M. COWLEY AND A. F. MOODIE, *Acta Crystallogr.* **10**, 609 (1957).
7. J. M. COWLEY AND A. F. MOODIE, *Proc. Roy. Soc. Ser. B* **70**, 497 (1957).
8. R. B. VON DREELE, L. EYRING, A. L. BOWMAN, AND J. L. YARNELL, *Acta Crystallogr.*, Sect. *B* **31**, 971 (1975).
9. M. Z. LOWENSTEIN, L. KHILBORG, K. H. LAU, J. M. HASCHKE, AND L. EYRING, *Nat. Bur. Stand. U.S. Spec. Publ.* **364**, 343 (1972).
10. S. IIJIMA, *Acta Crystallogr.*, Sect. *A* **29**, 18 (1973).
11. A. J. SKARNULIS, S. IIJIMA, AND J. M. COWLEY, *Acta Crystallogr.*, Sect. *A* **32**, 799 (1976).
12. P. GOODMAN AND A. F. MOODIE, *Acta Crystallogr.*, Sect. *A* **30**, 280 (1974).
13. P. L. FEJES, Ph.D. Dissertation, Arizona State University (1973).
14. M. R. THORNBER, D. J. M. BEVAN, AND J. GRAHAM. *Acta Crystallogr.*, Sect. *B* **24**, 1183 (1968).
15. G. R. ANSTIS, D. F. LYNCH, A. F. MOODIE, AND M. A. O'KEEFE, *Acta Crystallogr.*, Sect. *A* **29**, 138 (1973).